Structure and Physical Properties of a New 1:1 Cation-Radical Salt, ζ-(BEDT−TTF)PF_6

Hsiang-Lin Liu,[†] Liang-Kuei Chou,[‡] Khalil A. Abboud,[‡] Brian H. Ward,[‡] Gail E. Fanucci,[‡] Garrett E. Granroth,[†] Enric Canadell,[§] Mark W. Meisel,*[,†] Daniel R. Talham,*[,‡] and David B. Tanner*[,†]

Department of Physics, University of Florida, Gainesville, Florida 32611-8440; Department of Chemistry, University of Florida, Gainesville, Florida 32611-7200; and Institut de Ciència de Materials de Barcelona (CSIC), Campus de la UAB, E-08193 Bellaterra, Spain

Received March 10, 1997[⊗]

The synthesis, structural characterization, electrical transport, optical, and magnetic properties of a new cation-radical salt, bis(ethylenedithio)tetrathiafulvalene hexafluorophosphate, ζ-(BEDT−TTF)PF_6, are reported. The X-ray structure was determined at 298 K and at 173 K. The primary difference at the two temperatures is that the PF_6^- anions are disordered at 298 K and ordered at 173 K. At 298 K the salt is in the triclinic space group $P\bar{1}$ with crystallographic parameters $a = 6.2793(1)$ Å, $b = 7.3680(1)$ Å, $c = 9.9006(1)$ Å, $\alpha = 92.542(1)°$, $\beta = 93.255(1)°$, $\gamma = 98.763(1)°$, $vol = 451.33(1)$ Å^3. At 173 K the salt retains the same space group with parameters $a = 6.2293(1)$ Å, $b = 7.2633(2)$ Å, $c = 9.8662(2)$ Å, $\alpha = 92.898(1)°$, $\beta = 93.592(1)°$, $\gamma = 97.914(1)°$, $vol = 439.95(2)$ Å^3. Despite a crystal structure with uniform and segregated layers of donors and counterions, the room-temperature dc conductivity is rather low, $\sim 1.1 \times 10^{-4}$ Ω^{-1} cm^{-1}, and decreases rapidly upon cooling. Polarized reflectance measurements along the *a* axis of ζ-(BEDT−TTF)PF_6 provide evidence that the material is a Mott−Hubbard insulator with an effective on-site Coulomb interaction U_{eff} of 0.82 eV and a transfer matrix element *t* of 0.21 eV. An analysis of the infrared A_g modes yields a dimensionless electron−molecular−vibration coupling constant $\lambda \sim 0.1$. When the temperature is lowered, the activation energy for transport, the far-infrared phonons, and the magnetic susceptibility χ all exhibit an anomaly at ∼250 K which is related to the order/disorder transition of the PF_6^- counterions. In the low-temperature phase, the spectral weight of the three lowest A_g modes changes gradually, suggesting that the phase transition is close to second order. Finally, an exponential drop of χ occurs below 40 K, indicating the opening of a gap in the spin excitation spectrum. We suggest that this magnetic phase transition has structural aspects and can probably be associated with a spin-Peierls transition.

I. Introduction

Cation-radical salts of the organic donor molecule bis(ethylenedithio)tetrathiafulvalene (BEDT−TTF) have been of great interest since the 1983 report of superconductivity in the salt (BEDT−TTF)$_2ReO_4$.[1] At the time, BEDT−TTF was only the second molecule known to form the basis of organic superconductors. BEDT−TTF remains the most important organic donor molecule used in the preparation of new superconducting organic solids with over 50 known superconductors now reported.[2] Currently, the BEDT−TTF salt with the highest superconducting transition temperature is κ-(BEDT−TTF)$_2$Cu[N(CN)$_2$]Cl where $T_c = 12.8$ K under a pressure of 0.3 kbar.[3]

Most conducting and superconducting cation-radical salts in the BEDT−TTF family form with a 2:1 donor:anion stoichiometry with monovalent anions. In the 2:1 salts, the electronic band structure can be thought of as quarter-filled holelike when considering one BEDT−TTF molecule as the basis unit. In cases where the BEDT−TTF molecules are dimerized, the conduction band is split into two parts resulting in a one-half-filled band. While the most commonly studied organic cation-radical salts are those where the formal oxidation state of the donor is $+^1/_2$, other oxidation states of BEDT−TTF are known. In fact, cation-radical salts of BEDT−TTF with oxidation states as high as +2 have been isolated, showing that high-oxidation state salts of BEDT−TTF are stable.[4] In an effort to prepare BEDT−TTF cation-radical salts with differing degrees of band filling, we are currently pursuing additional examples of high-oxidation-state cation-radical salts.

The title compound, ζ-(BEDT−TTF)PF_6, is a new cation-radical salt with BEDT−TTF in the +1 oxidation state. There are several other known BEDT−TTF:PF_6

* To whom correspondence should be addressed.
[†] Department of Physics.
[‡] Department of Chemistry.
[§] CSIC.
[⊗] Abstract published in *Advance ACS Abstracts,* July 15, 1997.

(1) Parkin, S. S. P.; Engler, E. M.; Schumaker, R. R.; Lagier, R.; Lee, V. Y.; Scott, J. C.; Greene, R. J. *Phys. Rev. Lett.* **1983**, *50*, 270.
(2) Williams, J. M.; Ferraro, J. R.; Thorn, R. J.; Carlson, K. D.; Geiser, U.; Wang, H. H.; Kini, A. M.; Whangbo, M.-H. *Organic Superconductors (Including Fullerenes): Synthesis, Structure, Properties and Theory*; Prentice Hall: Englewood Cliffs, NJ, 1992.
(3) Williams, J. M.; Kini, A. M.; Wang, H. H.; Carlson, K. D.; Geiser, U.; Montgomery, L. K.; Pyrka, G. J.; Watkins, D. M.; Kommers, J. M.; Boryschuk, S. J.; Strieby Crouch, A. V.; Kwok, W. K.; Schirber, J. E.; Overmyer, D. L.; Jung, D.; Whangbo, M.-H. *Inorg. Chem.* **1990**, *29*, 3272.
(4) Chou, L.-K.; Quijada, M. A.; Clevenger, M. B.; de Oliveira, G. F.; Abboud, K. A.; Tanner, D. B.; Talham, D. R. *Chem. Mater.* **1995**, *7*, 531.

S0897-4756(97)00143-9 CCC: $14.00

salts including the 2:1 salts α-(BEDT−TTF)$_2$PF$_6$,[5] β-(BEDT−TTF)$_2$PF$_6$,[6] γ-(BEDT−TTF)$_2$PF$_6$,[7] (BEDT−TTF)$_2$PF$_6$·C$_4$H$_8$O$_2$,[8] and (BEDT−TTF)$_2$PF$_6$·ClCH$_2$COCl.[9] Previously reported 1:1 phases include a monoclinic (BEDT−TTF)PF$_6$ phase,[1] δ-(BEDT−TTF)PF$_6$,[10] ϵ-(BEDT−TTF)PF$_6$,[11] (BEDT−TTF)PF$_6$·$^1/_2$CH$_2$Cl$_2$,[12] and (BEDT−TTF)PF$_6$·$^1/_2$THF.[9] An interesting aspect of the structure of the new phase reported here is that there is one BEDT−TTF ion per unit cell, resulting in a donor ion network made up of discrete BEDT−TTF monocations with significant intermolecular interactions. In this article, we report the X-ray crystal structure and the transport, optical, and magnetic properties of ζ-(BEDT−TTF)PF$_6$. At room temperature the material is a semiconductor exhibiting charge localization due to Mott−Hubbard type interactions. At lower temperatures, two phase transitions are observed. Near 250 K there is a structural transition related to ordering of the anions. There is also a magnetic phase transition near 40 K that is probably of spin-Peierls origin.

II. Experimental Section

(A) Materials Synthesis. BEDT−TTF was prepared following the procedure described by Larsen and Lenoir.[13] BEDT−TTF (7 mg) was placed in the working electrode arm of a two-electrode H-cell containing a total of 33 mL of 1.0 × 10^{-2} M tetrabutylammonium hexafluorophosphate in 10% CS_2/CH_2Cl_2. A constant current density of 1.5 μA/cm^2 was maintained at room temperature between the platinum working and counter electrodes that were separated by two glass frits. Small black needles and plates were obtained upon harvesting after 10 days. ζ-(BEDT−TTF)PF$_6$ was not obtained if the solvents were degassed before use. When the solvents were degassed and distilled, other 1:1 phases, δ-(BEDT−TTF)PF$_6$[10] and ϵ-(BEDT−TTF)PF$_6$[11] predominated. We speculate that dissolved oxygen is necessary to form the ζ-(BEDT−TTF)PF$_6$ phase. The highest yields of ζ-(BEDT−TTF)PF$_6$ resulted when solvents were used as received from the vendor.

(B) X-ray Crystal Analysis. Data were collected at room temperature and at 173 K on a Siemens SMART PLATFORM equipped with a CCD area detector, and a graphite monochromator utilizing Mo Kα radiation (wavelength = 0.710 73 Å), and an LN_2 Siemens low-temperature device. Crystals were mounted on glass fibers using epoxy resin for the room-temperature crystal and Paratone N oil for the low-temperature crystal. Cell parameters were refined using the entire data set. A hemisphere of data (1321 frames) was collected using the ω-scan method (0.3° frame width). The first 50 frames were remeasured at the end of data collection to monitor instrument and crystal stability (maximum correction on I was <1%). ψ-scan absorption corrections were applied based on the entire data set.

Both structures were solved by Direct Methods in SHELXTL5[14] and refined using full-matrix least-squares on F^2. The non-H atoms were refined with anisotropic thermal parameters. All of the H atoms were included in the final cycle of refinement and refined without constraints. The PF_6^- unit is found to be disordered in the room-temperature structure and ordered in the low-temperature structure. Two sets of three F atoms (PF_6^- is located on a center of inversion) were refined, and the occupation factor of the major part refined to 0.69(2), and consequently the minor has an occupation factor of 0.31(2).

(C) Transport Techniques. The temperature-dependent (180−294 K) four-probe resistance was measured using an ac phase-sensitive technique. Needle-shaped crystals (typically 1.0 × 0.13 × 0.04 mm^3) were measured in this study. Narrow-gauge (0.02 mm diameter) gold wires were affixed to the crystal under a microscope using fast-drying gold paint. The sample was attached to a holder which fits onto the home-built low-temperature dipstick. A typical run was done by first cooling the sample to the lowest temperature and then taking the data while warming. Temperature reproducibility has been determined to be ±0.5 K or better over the temperature range measured.

(D) Optical Spectroscopy. Near-normal polarized reflectance measurements were made on single-crystal samples. Far-infrared and mid-infrared measurements were carried out on an Bruker 113v Fourier transform infrared spectrometer using a 4.2 K bolometer detector (30−600 cm^{-1}) and a B-doped Si photoconductor (450−4000 cm^{-1}). Wire grid polarizers on polyethylene and AgBr were used in the far- and mid-infrared, respectively. A Perkin-Elmer 16U grating spectrophotometer in conjunction with thermocouple, PbS, and Si detectors was used to measure the spectra in the infrared to the ultraviolet (1000−32000 cm^{-1}), using wire grid and dichroic polarizers. For low-temperature measurements, the sample was mounted in a continuous-flow helium cryostat equipped with a thermometer and heater near the cryostat tip, regulated by a temperature controller.

Experiments were performed with light polarized parallel and perpendicular to the maximum reflectance on the (001) crystal face, which was the only face large enough for the infrared studies. The initial reflectance reference was an aluminum mirror. To correct for size differences between sample and reference and to compensate for scattering losses, all samples were coated with a thin aluminum layer after the optical measurements were finished. The final corrected reflectance was obtained by ratioing the initial reflectance (no coating) to the reflectance of the coated sample and then multiplying the ratio by the reflectance of aluminum. After the reflectance spectra were measured, the optical properties were determined by Kramers−Kronig analysis.[15] Because an extremely large frequency region was covered, Kramers−Kronig analysis should provide reasonably accurate values for the optical constants. To perform these transformations, one needs to extrapolate the reflectance at both low and high frequencies. At very low frequencies the reflectance was assumed constant. Between the highest-frequency data point and 10^6 cm^{-1}, the reflectance was assumed to follow a power law of ω^{-1}; beyond this frequency range a free-electron-like behavior of ω^{-4} was used.

(E) Magnetic Measurements. The temperature dependence of the magnetic susceptibility was obtained from magnetization measurements in a standard commercial SQUID magnetometer. The samples were a set of randomly oriented single crystals with a total mass of 5.9 mg (sample 1) and 13.2 mg (sample 2). A gelcap and a plastic straw were used as the sample holder during the measurements. Samples 1 and 2 were zero-field-cooled to 2 K before a measuring field of 100 G or 1.0 kG was applied. Each data set was taken while warming the sample from the lowest temperature. The

(5) Kobayashi, H.; Kato, R.; Mori, T.; Kobayashi, A.; Sasaki, Y.; Saito, G.; Inokuchi, H. *Chem. Lett.* **1983**, 759.
(6) Kobayashi, H.; Mori, T.; Kato, R.; Kobayashi, A.; Sasaki, Y.; Saito, G.; Inokuchi, H. *Chem. Lett.* **1983**, 581.
(7) Bu, X.; Cisarova, I.; Coppens, P. *Acta Crystallogr.* **1992**, *C48*, 516.
(8) Bu, X.; Cisarova, I.; Coppens, P. *Acta Crystallogr.* **1992**, *C48*, 1563.
(9) Abbound, K. A.; Chou, L.-K.; Clevenger, M. B.; Oliveira, G. F.; Talham, D. R. *Acta Crystallogr.* **1995**, *C51*, 2356.
(10) Bu, X.; Cisarova, I.; Coppens, P. *Acta Crystallogr.* **1992**, *C48*, 1558.
(11) Bu, X.; Cisarova, I.; Coppens, P. *Acta Crystallogr.* **1992**, *C48*, 1562.
(12) Frère, P.; Carlier, R.; Boubekeur, K.; Gorgues, A.; Roncali, J.; Tallec, A.; Jubault, M.; Batail, P. *J. Chem. Soc., Chem. Commun.* **1994**, 2071.
(13) Larsen, J.; Lenoir, C. *Synthesis* **1988**, *2*, 134.
(14) Sheldrick, G. M.; *SHELXTL5*, Nicolet XRD Corporation, Madison, WI, 1995.
(15) Wooten, F. *Optical Properties of Solids*; Academic: New York, 1972.

Table 1. Crystallographic Data for ζ-(BEDT−TTF)PF_6 at 298 and at 173 K

	298 K	173 K
a (Å)	6.2793(1)	6.2293(1)
b (Å)	7.3680(1)	7.2633(2)
c (Å)	9.9006(1)	9.8662(2)
α (deg)	92.542(1)	93.898(1)
β (deg)	93.255(1)	93.592(1)
γ (deg)	98.763(1)	97.914(1)
vol (Å^3)	451.33(1)	439.95(2)
d_{calc}, g cm^{-3}	1.949	1.999
empirical formula	$C_{10}H_8S_8(PF)_6$	$C_{10}H_8S_8(PF)_6$
formula wt, g	529.61	529.61
crystal system	triclinic	triclinic
space group	$P\bar{1}$	$P\bar{1}$
Z	1	1
F(000), eletrons	265	265
crystal size (mm^3)	0.30 × 0.21 × 0.14	0.28 × 0.21 × 0.15
radiation, wavelength (Å)	Mo Kα, 0.710 73	
mode	*ω*-scan	
scan width and rate	0.3°/frame and 30 s/frame	
2*θ* range, deg	3−55	3−55
range of *hkl*	$-8 \le h \le 7$	$-7 \le h \le 7$
	$-9 \le k \le 19$	$-9 \le k \le 7$
	$-12 \le l \le 12$	$-12 \le l \le 12$
total reflns measd	3324	3274
unique reflections	1806	1773
absorption coeff μ(Mo Kα), mm^{-1}	1.129	1.158
refinement method	full-matrix least-squares on F^2	
S, goodness-of-fit	1.086	1.113
no. of variables	159	131
R_1/reflections	2.96/1728 > 2σ(*I*)	3.27/1773 > 2σ(*I*)
wR_2/reflections	7.41/1806	7.69/1773
R_{int} (%)	2.94	6.21
max shifted/esd	0.001	0.001
min peak in diff Fourier map (e Å^{-3})	−0.30	−0.61
max peak in diff Fourier map (e Å^{-3})	0.037	0.51

background signals arising from the gelcap and straw were measured independently and subtracted from the results.

Electron spin resonance (ESR) spectra were recorded between 4 and 298 K using a Bruker ER-200 spectrometer equipped with an Oxford Instruments ITC 503 temperature controller and ESR 900 flow cryostat. A ζ-(BEDT−TTF)PF_6 single crystal (1.25 × 1.0 × 0.06 mm^3) was selected and mounted on a cut edge of a quartz rod; rotation was achieved using a home-built goniometer. The sample was first oriented vertically in the microwave cavity. The 0° and 90° orientations corresponded to the parallel and perpendicular alignments, respectively, of the crystal plane normal (*c**) with respect to the static magnetic field. On the second run, the sample was oriented horizontally in the microwave cavity, that is, the microwave electric field is parallel to the crystal plane (*ab* plane), and the static magnetic field perpendicular to the *c** axis. The temperature-dependent electron spin resonance data were obtained at 9.26 GHz with 100 kHz field modulation.

III. Results

(A) Crystal Structure. ζ-(BEDT−TTF)PF_6 crystallizes in the triclinic system *P*1̄. Crystallographic data for both room temperature and 173 K are presented in Table 1. Atomic coordinates and equivalent isotropic displacement parameters are listed in Table 2.

Like many BEDT−TTF cation-radical salts, two-dimensional sheets of the cation-radicals are separated by sheets of the counterions. The anion and cation sheets are oriented parallel to the *ab* plane shown in Figure 1. A consequence of the low crystal symmetry is that the principal molecular axes of the BEDT−TTF ion do not correspond with any of the crystallographic axes. In the low-temperature crystal structure, the long

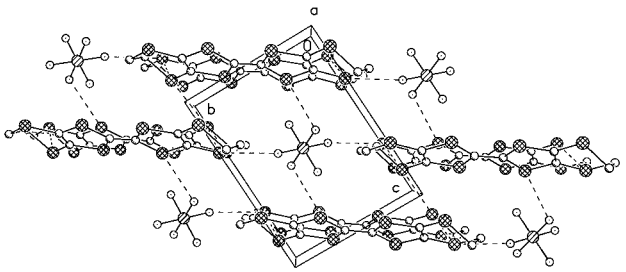

Figure 1. View down the *a*-axis of ζ-(BEDT−TTF)PF_6 at room temperature. The dashed lines represent nonbonding interactions. Disorder in the anion network has been omitted for clarity.

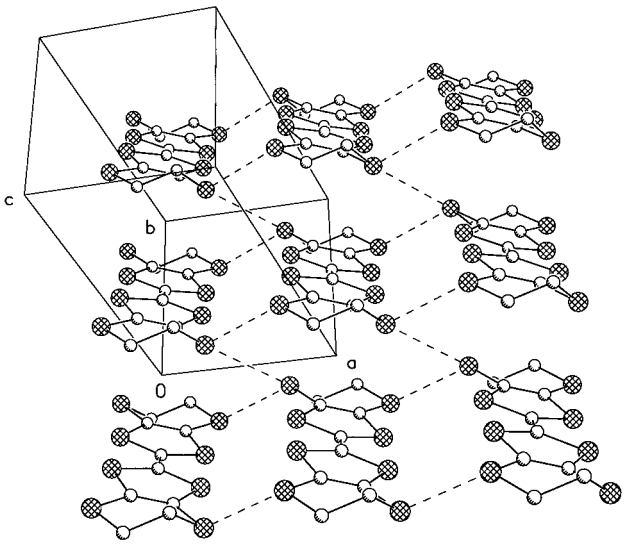

Figure 2. View along the long axis of the (BEDT−TTF)$^+$ ion showing the packing arrangement of the BEDT−TTF units at room temperature. PF_6 anions have been removed for clarity. The dashed lines represent S−S distances that are less than the sum of the van der Waals radii.

axis of the BEDT−TTF cation forms angles of 74°, 34°, and 56° with the *a*, *b*, and *c* axes, respectively. At room temperature, the PF_6^- ion is located on a center of inversion and is rotationally disordered. The structure was refined with two sets of three F atoms having occupation factors of 0.69(2) and 0.31(2). The PF_6^- ions are ordered in the low-temperature structure.

Figure 2 shows the molecular arrangement within the BEDT−TTF sheets. Along the *b*-axis, molecules appear to stack face-to-face, but because the molecules are slipped relative to each other, overlap is poor. The closest intermolecular nonbonding orbital interactions are the nearly side-by-side contacts between outer-ring sulfur atoms on adjacent molecules along the *a* axis. The S−S contacts are 3.525 Å at room temperature, decreasing to 3.470 Å at 173 K. There is also a short S−S contact along the *ab* direction between the outer-ring sulfur atoms at opposite ends of the molecules. Additionally, a number of nonbonding interactions are also observed involving the BEDT−TTF donors and PF_6^- ions at both room temperature and 173 K.

The crystal packing of the monocation salt ζ-(BEDT−TTF)PF_6 closely resembles that in δ-(BEDT−TTF)PF_6[10] where two-dimensional sheets of donor molecules are also separated by layers of PF_6^- counterions. In ζ-(BEDT−TTF)PF_6, the donor ion sheets are comprised of discrete BEDT−TTF$^+$ monomers, while in the δ-phase there is increased face-to-face overlap, and the donor

Table 2. Atomic Coordinates ($\times 10^4$) and Equivalent Isotropic Displacement Parameters (Å$^2 \times 10^3$) for ζ-(BEDT−TTF)PF_6 at 298 and 173 K (U_{eq} Defined as One-Third of the Trace of the Orthogonalized U_{ij} Tensor)[a]

	298 K				173 K			
atom	*x*	*y*	*z*	U_{eq}	*x*	*y*	*z*	U_{eq}
S(1)	1459(1)	6637(1)	8422(1)	41(1)	1424(1)	6620(1)	8421(1)	21(1)
S(2)	−2455(1)	6782(1)	9834(1)	42(1)	−2503(1)	6808(1)	9847(1)	21(1)
S(3)	1264(1)	9988(1)	6947(1)	48(1)	1121(1)	9944(1)	6915(1)	23(1)
S(4)	−3544(1)	10082(1)	8529(1)	48(1)	−3730(1)	10068(1)	8511(1)	24(1)
C(1)	−215(3)	5734(3)	9621(2)	36(1)	−230(3)	5734(3)	9632(2)	19(1)
C(2)	87(3)	8468(3)	8088(2)	34(1)	−9(3)	8456(3)	8080(2)	18(1)
C(3)	−1744(3)	8523(3)	8742(2)	35(1)	−1850(3)	8527(3)	8735(2)	18(1)
C(4)	−658(4)	11564(3)	6727(2)	43(1)	−828(3)	11577(3)	6750(2)	21(1)
C(5)	−2974(4)	10698(3)	6823(2)	43(1)	−3153(3)	10684(3)	6812(2)	21(1)
P	5000	5000	5000	39(1)	5000	5000	5000	19(1)
F(1)	3532(16)	6419(10)	5481(8)	99(2)	3651(3)	6559(2)	5579(2)	39(1)
F(2)	3395(7)	3315(7)	5419(11)	103(2)	3274(3)	3389(2)	5477(2)	48(1)
F(3)	6169(16)	5087(7)	6448(5)	112(3)	3660(3)	4908(2)	3562(2)	50(1)
F(1′)	4090(34)	6685(17)	5597(19)	91(5)				
F(2′)	4047(31)	3918(19)	6206(15)	99(6)				
F(3′)	2848(17)	4500(23)	4185(22)	143(6)				

[a] For anisotropic atoms, the *U* value is U_{eq}, calculated as $U_{eq} = {}^1/_3\sum_i\sum_j U_{ij}a_i^*a_j^*A_{ij}$ where A_{ij} is the dot product of the *i*th and *j*th direct-space unit-cell vectors.

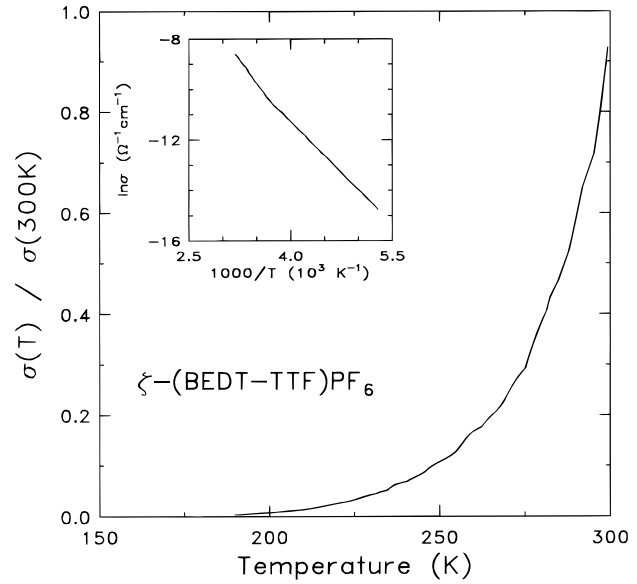

Figure 3. dc conductivity normalized by its room-temperature value ($(1.1 \pm 0.1) \times 10^{-4}$ Ω^{-1} cm^{-1}) for ζ-(BEDT−TTF)PF_6 as a function of temperature. Inset shows the plot of ln σ versus 1000/*T*.

ions are strongly dimerized. At room temperature, δ-(BEDT−TTF)PF_6 is diamagnetic while ζ-(BEDT−TTF)PF_6 is paramagnetic.

(B) Transport Properties. The dc electrical conductivity is shown in Figure 3. ζ-(BEDT−TTF)PF_6 behaves as a semiconductor with a room-temperature conductivity of $1.1 \times 10^{-4} \pm 0.1 \times 10^{-4}$ Ω^{-1} cm^{-1}. The conductivity decreases rapidly from its 300 K value as the temperature is decreased. The typical temperature-dependent conductivity of a semiconductor may be expressed as

$$\sigma(T) = \sigma_0 e^{-E_g/2k_BT} \quad (1)$$

where E_g is the semiconductor gap. However, a plot of ln σ versus 1/*T* does not obey a single linear relationship. Two different linear fits are obtained above and below a crossover point at 250 K with thermal activation energies $E_a = E_g/2$ of 0.30 eV at high *T* and 0.23 eV at low *T*. The smaller E_a at low temperature is probably due to subtle structural changes within the BEDT−TTF planes that accompany ordering of the PF_6^- anions.

As previously mentioned, three other examples of BEDT−TTF cation-radical salts have the same counterion and stoichiometry as ζ-(BEDT−TTF)PF_6. There are no reports of conductivity measurements in those salts. On the other hand, conductivity has been measured in the 2:1 salts, α-(BEDT−TTF)$_2PF_6$ and β-(BEDT−TTF)$_2PF_6$. The α phase is a one-dimensional semiconductor at room temperature with $\sigma \sim 0.1$ Ω^{-1} cm^{-1} and an activation energy of ∼0.05 eV.[5] β-(BEDT−TTF)$_2PF_6$ is metallic with $\sigma \sim 10$ Ω^{-1} cm^{-1} near room temperature and shows the metal−insulator transition at 297 K.[6] The conductivity of ζ-(BEDT−TTF)PF_6 is comparable to that of other 1:1 organic conductors with integer charge on the molecules. For example, the electrical conductivities of the alkali-TCNQ (TCNQ = tetracyanoquinodimethane) salts exhibit semiconducting behavior; $\sigma \sim 10^{-4}$−10^{-5} Ω^{-1} cm^{-1} with activation energies $E_a \sim 0.35$ eV for Li−, Na−, and K−TCNQ and 0.18 eV for Cs−TCNQ.[16] The series of conducting salts based on [M(dmit)$_2$] molecules (dmit = 1,3-dithiole-2-thione-4,5-dithiolato), (Me_4N)[Ni(dmit)$_2$], (Et_4N)[Ni(dmit)$_2$], (Pr_4N)[Ni(dmit)$_2$], (Bu_4N)[Ni(dmit)$_2$], and (Bu_4N)[Pd(dmit)$_2$], all display room-temperature conductivities in the range 5×10^{-9} to 4×10^{-5} Ω^{-1} cm^{-1} with activation energies between 0.1 and 0.5 eV.[17]

(C) Optical Results. *(1) Room-Temperature Spectra.* Figure 4 shows the room-temperature reflectance on the (001) face over the spectral range 100−32000 cm^{-1}. Data are shown for polarizations parallel and perpendicular to the direction of maximum reflectance (R_{max}). R_{max} is polarized purely along the crystallographic *a*-axis, which is the direction of greatest intermolecular interaction. For the electric field polarized parallel to the *a*-axis, the spectrum displays a series of narrow structures associated with molecular vibrations at low frequencies and a broad maximum peak along with several weak features from electronic transitions at higher frequencies. In contrast, perpendicular to the *a*-axis, the reflectance is low (∼5%) and almost dispersionless.

The real part of the conductivity $\sigma_1(\omega)$, obtained from a Kramers−Kronig analysis of the reflectance, is shown in Figure 5. The conductivity in the *a* direction is clearly seen to increase for frequencies above 5000 cm^{-1}

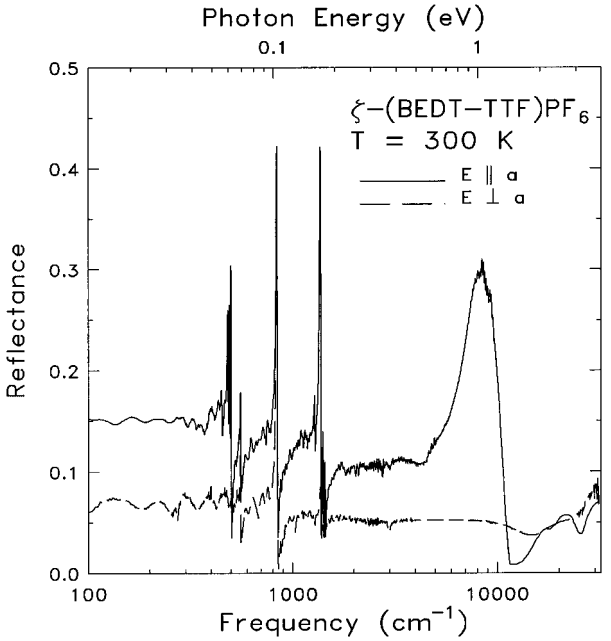

Figure 4. Room-temperature reflectance of ζ-(BEDT−TTF)-PF_6 with light polarized along the *a*-axis reflectance direction (solid line) and perpendicular (dashed line) to it on the (001) crystal face.

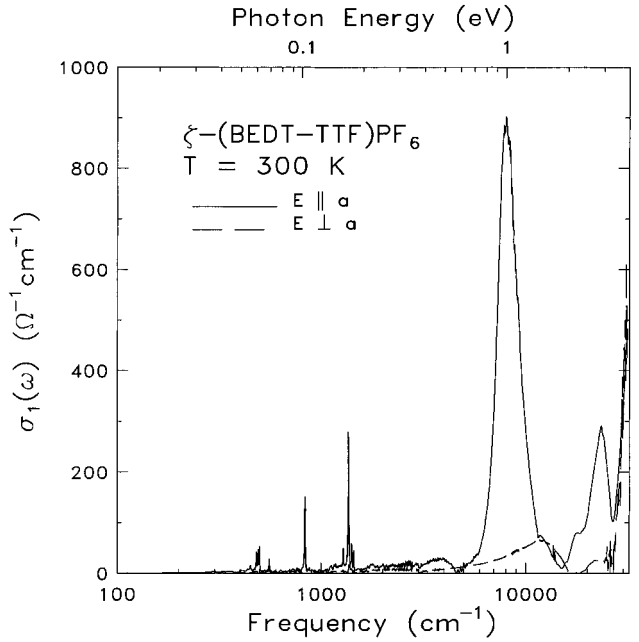

Figure 5. Frequency-dependent conductivity obtained by Kramers−Kronig analysis of the room-temperature reflectance of ζ-(BEDT−TTF)PF_6. The conductivity is shown for parallel and perpendicular to the *a*-axis.

and reaches a peak around 8000 cm^{-1}. The onset frequency roughly corresponds to the energy gap deduced from the activation energy observed in the transport measurement ($E_g \sim 0.6$ eV = 4840 cm^{-1}). This absorption band contains the majority of the oscillator strength. Other weak, broad electronic structures appear between 17 500 and 25 000 cm^{-1}. At low frequencies, the spectrum exhibits many sharp vibrational features, most of which can be attributed to infrared-active BEDT−TTF modes as well as modes of the PF_6^- anions. Additional vibrational structure is located near the frequencies of the totally symmetric A_g modes of the BEDT−TTF molecule, which are supposed to be infrared

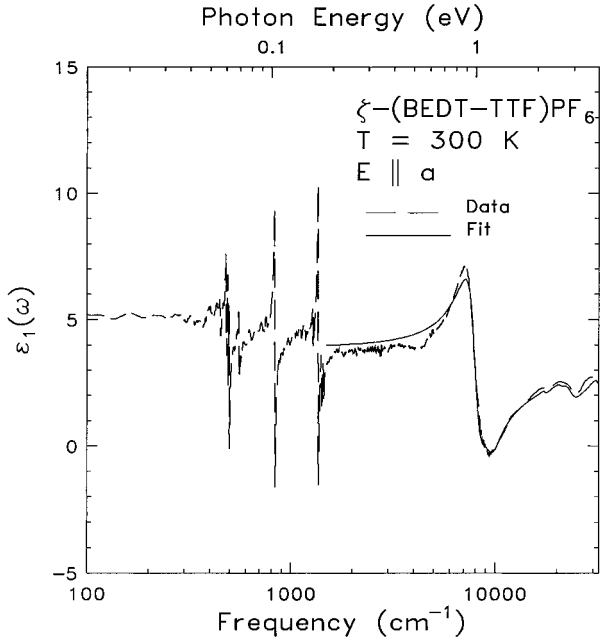

Figure 6. Real part of the dielectric function (dashed line) obtained by Kramers−Kronig analysis of the room-temperature reflectance of ζ-(BEDT−TTF)PF_6 along the *a* direction. Lorentz fit to the reflectance data is shown as the solid lines, and the fitting parameters of eq 2 are given in Table 3.

inactive; their activation originates from the coupling of electrons to these modes.[18−20] The $\sigma_1(\omega)$ for polarization perpendicular to the *a* direction is rather flat. Indeed, the extremely anisotropic behavior in the electronic properties of ζ-(BEDT−TTF)PF_6 have been observed for many other organic materials as well.[21] Only at high frequencies, above 10 000 cm^{-1}, is there weak electronic absorption.

The real part of the dielectric function, $\epsilon_1(\omega)$, along the *a* direction is presented in Figure 6. For frequencies near the conductivity maximum, the dielectric function displays the usual derivative-like structure. By extrapolating the low-frequency far-infrared data to zero frequency, an estimate of the static dielectric constant of $\epsilon(0) \sim 5$ is obtained. We also estimate the high-frequency (above 10 000 cm^{-1}) dielectric constant, ϵ_∞, to be 2.05. A fit of the reflectance [or the complex dielectric function $\epsilon(\omega) = \epsilon_1(\omega) + i\epsilon_2(\omega)$] from the near-infrared to ultraviolet regions to a sum of Lorentz oscillators is also shown. The model dielectric function is[15]

$$\epsilon(\omega) = \sum_j \frac{\omega_{pj}^2}{\omega_j^2 - \omega^2 - i\omega\gamma_j} + \epsilon_\infty \qquad (2)$$

where ω_{pj}, ω_j, and γ_j are the oscillator strength, center frequency, and scattering rate of the *j*th transition and ϵ_∞ represents the other higher frequency contributions to the dielectric function. The parameters obtained for

(16) Vegter, J. G.; Hibma, T.; Kommandeur, J. *Chem. Phys. Lett.* **1969**, *3*, 427.
(17) Kramer, G. J.; Jol, J. C.; Brom, H. B.; Groeneve, L. R.; Reedijk, J. *J. Phys. C* **1988**, *21*, 4591.
(18) Rice, M. J. *Phys. Rev. Lett.* **1976**, *37*, 36.
(19) Rice, M. J. *Solid State Commun.* **1979**, *31*, 93.
(20) Rice, M. J.; Yartsev, V. M.; Jacobsen, C. S. *Phys. Rev. B* **1980**, *21*, 3437.
(21) Tanner, D. B. *Extended Linear Chain Compounds*; Miller, J. S., Ed.; Plenum: New York, 1982; Vol. 2, Chapter 5.

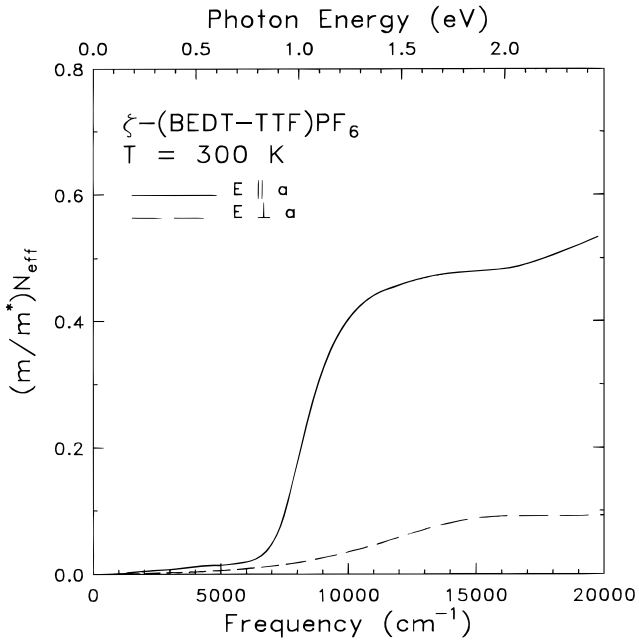

Figure 7. Result of the partial sum rule analysis for ζ-(BEDT−TTF)PF_6 with polarization parallel and perpendicular to the *a*-axis; see eq 3.

Table 3. Parameters of Lorentz Fit to the *a*-Axis Reflectance of ζ-(BEDT−TTF)PF_6 (See Figure 6)[a]

oscillators	ω_{pj} (cm^{-1})	ω_j (cm^{-1})	γ_j (cm^{-1})
1	9179	7990	1605
2	4713	9310	1793
3	1420	17500	852
4	2570	20860	1856
5	7700	23390	3928
6	14116	32900	3983

[a] $\epsilon_\infty = 2.05$.

Table 4. Values of the Fitting Parameters to the Static Susceptibility of ζ-(BEDT−TTF)PF_6 (See Figure 9)

sample	T_{sp} (K)	Δ(0) (K)	J (K)	mult	χ(0) (emu/mol)	C (emu K/mol)
1 in 1 kG	40	70	160	0.12	7.5×10^{-5}	7×10^{-5}
2 in 1 kG	43	76	172	0.10	1.4×10^{-4}	4×10^{-4}
2 in 100 G	43	76	172	0.18	1.9×10^{-4}	6×10^{-4}

our sample are listed in Table 3. The results for the fit are compared to $\epsilon_1(\omega)$ in Figure 6.

Additional information about the electronic structure of ζ-(BEDT−TTF)PF_6 can be extracted from the oscillator strength sum rule.[15] The effective number of electrons participating in optical transitions for energies less than $\hbar\omega$ is given by

$$\left[\frac{m}{m^*}\right]N_{\text{eff}}(\omega) = \frac{2mV_{\text{cell}}}{\pi e^2}\int_0^{\omega}\sigma_1(\omega')\,d\omega' \qquad (3)$$

where m^* is the effective mass of the carriers, m the free-electron mass, and V_{cell} the unit cell volume. A plot of this function vs frequency is shown in Figure 7. In the *a* direction, $(m/m^*)N_{\text{eff}}$ is small until 5000−6000 cm^{-1}, where it rises very rapidly and begins to level off, and then rises again above the onset of the high-frequency electronic bands. From the plateau value (∼0.47) of $(m/m^*)N_{\text{eff}}$, assuming that the carrier density is equal to the number density of $BEDT-TTF^+$ molecules, we estimate $m^* = 2.13m$. In the polarization perpendicular to the *a* direction, $(m/m^*)N_{\text{eff}}$ is close to zero in the infrared but rises at higher frequencies. The anisotropy ratio of the effective mass, $m^*_\perp/m^*_\parallel = 4.9$, is larger than the corresponding values in metallic BEDT−TTF salts, where values of 3.5, 2.1, and 1.4 are reported for β-$(BEDT-TTF)_2I_3$,[22] θ-$(BEDT-TTF)_2I_3$,[23] and κ-$(BEDT-TTF)_2I_3$,[24] respectively.

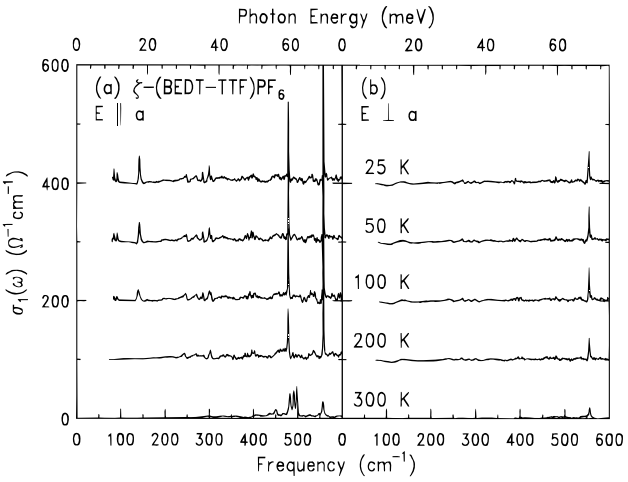

Figure 8. Detailed temperature dependence of the far-infrared conductivities of ζ-(BEDT−TTF)PF_6 for both polarizations. The curves have been offset for clarity.

(2) Temperature Dependence in the Far Infrared. To compare the high-temperature and low-temperature phases in ζ-(BEDT−TTF)PF_6, Figure 8 shows the far-infrared conductivity spectra for both polarizations at several temperatures. We observe no significant temperature variation perpendicular to the *a* axis, but the character of the frequency-dependent conductivities along the *a* axis is a strong function of temperature, indicating that important changes occur in the lattice and electronic structures as the result of the 250 K PF_6^- order/disorder transition.

(D) Magnetic Properties. *(1) Magnetic Susceptibility.* The temperature dependence of the magnetic susceptibility of sample 1 is plotted in Figure 9. Similar results were obtained for sample 2. After correction for the core diamagnetic component calculated using Pascal's constants ($\chi_{\text{core}} = (1.4 \pm 0.2) \times 10^{-4}$ emu/mol),[25] a room-temperature susceptibility of 3.4×10^{-4} emu/mol was determined. Over the entire temperature region, the static susceptibility at first decreases gradually from room temperature to 200 K and then shows little variation with temperature down to 40 K, while another weaker change of slope is observed at 130 K. Below 40 K, χ falls off rapidly. However, at temperatures lower than 10 K, the data are dominated by a Curie-like tail, presumably arising from magnetic defects or impurities. This region is shown on an expanded scale in the inset.

(2) ESR Spectra. The X-band ESR signal of ζ-(BEDT−TTF)PF_6 was measured as a function of orientation and temperature. Figure 10 shows the temperature dependence of the peak-to-peak derivative ESR line widths (ΔH), recorded with the microwave field parallel, and

(22) Tajima, H.; Yakushi, K.; Kuroda, H.; Saito, G. *Solid State Commun.* **1986**, *56*, 159.
(23) Yakushi, K.; Tajima, H.; Kanbara, H.; Tamura, M.; Kuroda, H.; Saito, G.; Kobayahi, H.; Kato, R.; Kobayashi, A. In *Proceedings of the Fifteenth Yamada Conference on Physics and Chemistry of Quasi One-Dimensional Conductors, Physica B* **1986**, *143*, 463.
(24) Kuroda, H.; Yakushi, K.; Tajima, H.; Ugawa, A.; Tamura, M.; Okawa, Y.; Kobayashi, A. *Synth. Met.* **1988**, *27*, A491.
(25) Mabbs, F. E.; Machin, D. J. *Magn. Trans. Met. Complexes* **1973**.

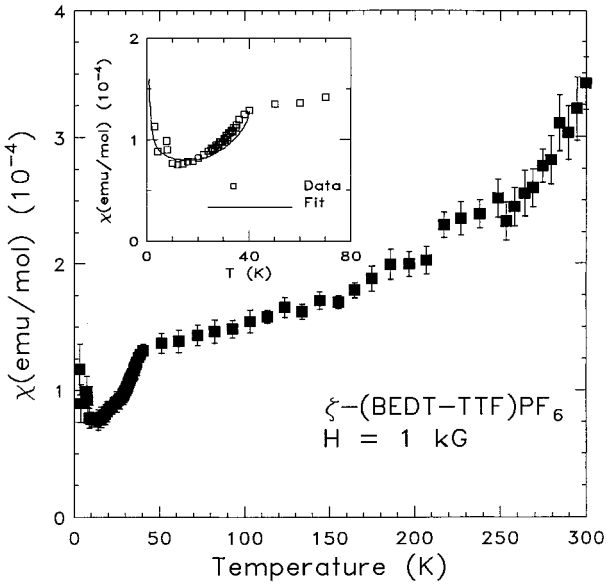

Figure 9. Temperature dependence of the magnetic susceptibility of ζ-(BEDT−TTF)PF_6, sample 1. The solid line in the inset is the calculated susceptibility as outlined in the text with the parameters given in Table 4.

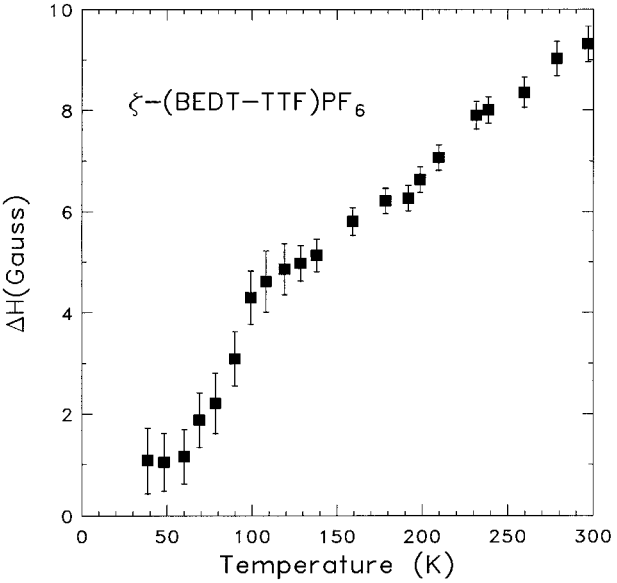

Figure 10. Temperature dependence of the ESR peak-to-peak line widths for ζ-(BEDT−TTF)PF_6.

the static magnetic field aligned perpendicular, to the face of the platelike crystals. The maximum peak-to-peak line width at room temperature is 9.4 G and then ΔH decreases nearly monotonically to about 4.0 G at 100 K. Below 100 K the line width decreases rapidly to a minimum of 1.4 G near 30 K, at which point there is no ESR signal detected as the temperature was lowered further. The loss of the ESR intensity is observed in all crystallographic directions at $T < 30$ K. The g value of ζ-(BEDT−TTF)PF_6 is almost temperature independent with deviations of only ±0.002 from 2.010 between 300 and 30 K.

IV. Discussion

Cation-radical salts are a class of compounds that display many interesting aspects of low-dimensional physics. It is generally accepted that the chemical identity of the donor cation and the stoichiometry of the salts determines the population of the conduction band. In these materials, interactions involving unpaired electrons in the highest occupied molecular orbital (HOMO) have especially important consequences. The tight-binding model is often used to obtain a band structure from the overlap integrals of molecular orbitals, while the extended Hubbard model describes the transfer integral between nearest-neighbor sites t, the on-site Coulomb repulsion energy U, and the interaction of electrons on nearest-neighbor sites V. In the case of simple 1:1 salts, such as ζ-(BEDT−TTF)PF_6 or other compounds,[9−11] there is one unpaired electron on each BEDT−TTF molecule. Because of the strong electron−electron Coulomb interaction U, the electrons are unlikely to doubly occupy sites. Hence, the tight-binding band is split into two bands, separated by a wide gap on the order of U. Electronically, they are often referred to as Mott−Hubbard insulators and consist of either completely filled or completely empty bands. The interaction localizes the electrons, giving an activated electrical conduction. Finally, the electron−electron correlation effects (the size of U and V) relative to the bandwidth $4t$ are also important considerations in the behavior of many quasi-one-dimensional charge-transfer salts.

(A) Electronic Features in the Optical Spectrum. We begin with the frequency-dependent conductivity, $\sigma_1(\omega)$, of ζ-(BEDT−TTF)PF_6, which is shown in Figure 5, and the parameters given in Table 3. The spectral features in the a direction consist of one strong absorption at ∼8000 cm^{-1}, which can be attributed to the electronic charge transfer between two radical BEDT−TTF cations: BEDT−TTF^+ + BEDT−TTF^+ → BEDT−TTF^0 + BEDT−TTF^{2+}. The large oscillator strength of this band indicates that a charge-transfer process takes place predominantly between the adjacent BEDT−TTF donors. In this situation, a theoretical description of the electronic interactions within a dimer by Harris and Lange[26] and by Rice[27] is a fair approximation. The model is just the Hubbard model restricted to a dimer. The charge-transfer excitation occurs at photon energy

$$\hbar\omega_{ct} = \frac{U_{eff}}{2} + \left(\frac{U_{eff}^2}{4} + 4t^2\right)^{1/2} \qquad (4)$$

The oscillator strength sum rule applied to this system provides a second relation for U_{eff} and t:

$$\int_{ct}\sigma_1(\omega)\,d\omega = \frac{\pi n_a e^2 a^2}{\hbar^2}\frac{2t^2}{(U_{eff}^2/4 + 4t^2)^{1/2}} \qquad (5)$$

where n_a is the number density of dimers and a the intradimer spacing. Analysis of the ζ-(BEDT−TTF)PF_6 data using this model gives values for the effective on-site Coulomb energy, $U_{eff} = U - V \sim 0.82$ eV and the transfer integral $t \sim 0.21$ eV. Assuming V is small, the Coulomb repulsion energy of ζ-(BEDT−TTF)PF_6 is comparable to typical values of $U \sim 1$ eV obtained for other charge-transfer salts.[21] Additionally, because

(26) Harris, A. B.; Lange, R. V. *Phys. Rev.* **1967**, *157*, 295.
(27) Rice, M. J. *Solid State Commun.* **1979**, *31*, 93.

$U \sim 4t$, ζ-(BEDT−TTF)PF_6 falls into the intermediate-to-strong Coulomb coupling regime.

For the electric field polarized perpendicular to the *a*-axis, two absorption bands at ∼13 000 and 22 000 cm^{-1} are thought to be intramolecular localized excitations or molecular excitons, in reasonable agreement with those observed in the solution spectra of the BEDT−TTF monocation.[4] Note that these two electronic transitions are also seen in the parallel polarization on account of the triclinic space group and the large angles between the molecular plane and the crystallographic axes.

To understand better the electronic structure of ζ-(BEDT−TTF)PF_6, the band structure was calculated using an extended Hückel type Hamiltonian[28] with a modified Wolfsberg−Helmholz formula to evaluate the nondiagonal H_{ij}' matrix element[29] and a double-ζ basis set.[30] There are three different types of HOMO−HOMO interactions: those along the *a* axis (S−S = 3.525 Å (×2), 3.716 Å (×2), 3.855 Å), *b* axis (S−S = 3.822 and 3.859 Å), and the diagonal component within the *ab* plane (S−S = 3.523 Å). The associated β interaction energies[31] are 0.196, 0.086, and 0.008 eV, respectively. These interaction energies are a measure of the strength of the interaction between a pair of BEDT−TTF HOMOs on adjacent sites of the crystal along the *a*, *b*, and *ab* directions, respectively. We note that the value for the *a*-axis β interaction energy (0.196 eV) is significant in comparison with many BEDT−TTF metallic salts where, for example, the largest β is around 0.3 eV. It is also worth mentioning that the interaction along the diagonal direction of the *ab* plane is weak despite the very short S−S contact. This result is a reminder of the importance of discussing the strength of the intermolecular interactions, as far as the transport properties are concerned, on the basis of $\beta_{HOMO-HOMO}$ interaction energies and not solely on the basis of short S−S contacts. The calculation suggests that the electrons on the BEDT−TTF donors are mainly confined to the stacks formed along the *a* axis, which is consistent with the observed optical properties. However, the *b* axis β energy is only about 2 times smaller than that along the *a* direction. This would favor the arrangement of BEDT−TTF units as a series of step chains along the *a* axis coupled weakly along the *b* axis. The fact that the interactions are not negligible is clear when looking at the dispersion of the HOMO band. Although the band structure has less meaning in a localized system, it gives an idea of the strength of the interactions in the lattice. For metallic BEDT−TTF salts, the total dispersion of the HOMO bands is typically around 1.2 eV which is not far from the value of 0.75 eV calculated for ζ-(BEDT−TTF)PF_6. With such a bandwidth for a single-band system, the salt could well have been a metal. Thus, the semiconducting behavior of ζ-(BEDT−TTF)PF_6 must be from the strong electron−electron correlation effects.

(B) Vibrational Spectra. There are three different phenomena seen in the infrared spectral region, where the vibrational features of the ζ-(BEDT−TTF)PF_6 crystal occur. First, there is strong activation of the A_g modes of the BEDT−TTF molecule for light polarized along the *a* axis. Second, there is interesting temperature dependence to the PF_6 vibrations at ∼556 and 883 cm^{-1}. Third, we observe many weaker phonon structures for polarization perpendicular to the *a* axis that seem to fit quite well into the pattern of the ordinary infrared-active modes. The C−H stretching $B_{1u}(\nu_{26})$ is resolved at ∼2920 cm^{-1}. The features near 1445 and 1411 cm^{-1} should correspond to C=C stretching $B_{1u}(\nu_{27})$ and C−H bending $B_{2u}(\nu_{45})$. More than likely there is another C−H bending $B_{1u}(\nu_{28})$ at ∼1379 cm^{-1}. There is a band at ∼1283 cm^{-1} which is related to complex C−S motion $B_{1u}(\nu_{29})$. The feature centered around 500 cm^{-1} is probably C−S bending $B_{1u}(\nu_{34})$.

We discuss the first and second of these effects in the following sections.

(C) Electron−Phonon Coupling. *(1) Room-Temperature Data.* Among the most prominent and interesting spectral features of BEDT−TTF charge-transfer salts are the in-plane A_g modes of the BEDT−TTF molecule, activated by coupling to the charge-transfer excitations.[32−34] Thirteen out of the expected seventeen A_g modes are observed in the *a* axis spectrum of ζ-(BEDT−TTF)PF_6, most with relatively strong intensity. This interaction has been previously observed in the infrared spectra of many other conducting and semiconducting BEDT−TTF salts.[32,35−40] The features have been interpreted with the help of the microscopic theories of electron−molecular−vibration (EMV) linear interactions in the one-dimensional organic solid state given by Rice and co-workers, the phase phonon theory[18] and dimer models.[19,20] Consequently, we analyze the conductivity spectrum of ζ-(BEDT−TTF)PF_6 in terms of an isolated, half-filled, dimer model.[19]

In this model, the frequency-dependent conductivity is

$$\sigma(\omega) = -\left(\frac{i\omega e^2 a^2 N}{4V_{cell}}\right)\left(\frac{\psi(\omega)}{1 - D(\omega)\psi(\omega)/\psi(0)}\right) \qquad (6)$$

where *a* is the dimer separation, *N* is the number of dimers per unit cell, and V_{cell} is the volume of the unit cell. The quantity $D(\omega)$ is the phonon propagator

(28) Hoffmann, R. *J. Chem. Phys.* **1963**, *39*, 1397.
(29) Ammeter, J.; Bürgi, H.-B.; Thibeault, J.; Hoffmann, R. *J. Am. Chem. Soc.* **1978**, *100*, 3686.
(30) Clementi, E.; Roetti, C. *At. Nucl. Data Tables* **1974**, *14*, 177.
(31) Whangbo, M.-H.; Williams, J. M.; Leung, P. C. W.; Beno, M. A.; Emge, T. J.; Wang, H. H. *Inorg. Chem.* **1985**, *24*, 3500. (b) Since overlap is explicitly included in extended Hückel calculations, these interaction energies (β) should not be confused with the conventional transfer integrals (*t*). Although the two quantities are obviously related and have the same physical meaning, the absolute values of the interaction energies are somewhat larger than those of the transfer integrals.
(32) Meneghetti, M.; Bozio, R.; Pecile, C. *J. Phys. (Paris)* **1986**, *47*, 1377.
(33) Kozlov, M. E.; Pokhodnia, K. I.; Yurchenko, A. A. *Spectrochim. Acta* **1987**, *43A*, 323.
(34) Kozlov, M. E.; Pokhodnia, K. I.; Yurchenko, A. A. *Spectrochim. Acta* **1989**, *45A*, 437.
(35) Ferraro, J. R.; Wang, H. H.; Ryan, J.; Williams, J. M. *Appl. Spectrosc.* **1987**, *41*, 1377.
(36) Jacobsen, C. S.; Tanner, D. B.; Williams, J. M.; Geiser, U.; Wang, H. H. *Phys. Rev. B* **1987**, *35*, 9605.
(37) Kornelsen, K.; Eldridge, J. E.; Homes, C. C.; Wang, H. H.; Williams, J. M. *Solid State Commun.* **1989**, *72*, 475.
(38) Kornelsen, K.; Eldridge, J. E.; Wang, H. H.; Williams, J. M. *Phys. Rev. B* **1991**, *44*, 5235.
(39) Eldridge, J. E.; Kornelsen, K.; Wang, H. H.; Williams, J. M.; Crouch, A. V. S.; Watkins, D. M. *Solid State Chem.* **1991**, *79*, 583.
(40) Drozdova, O.; Semkin, V. N.; Vlasova, R. M.; Kushch, N. D.; Yagubskii, E. B. *Synth. Met.* **1994**, *64*, 17.

$$D(\omega) = \sum_n \frac{\lambda_n {\omega_n}^2}{{\omega_n}^2 - \omega^2 - i\omega\gamma_n} \quad (7)$$

with λ_n the dimensionless electron−phonon coupling constant, ω_n the unperturbed frequency, and γ_n the phonon line width for the nth A_g mode. $\psi(\omega)$ is the reduced electronic polarizability:

$$\psi(\omega) = \frac{16t/({U_{\text{eff}}}^2/4 + 4t^2)^{1/2}}{{\omega_{\text{ct}}}^2 - \omega^2 - i\omega\gamma_{\text{e}}} \quad (8)$$

where ω_{ct} is frequency and γ_{e} is the line width of the electronic charge-transfer excitation. Taking the zero-frequency limit of the above expression, we find

$$\psi(0) = \frac{16t}{{\omega_{\text{ct}}}^2\left(\frac{{U_{\text{eff}}}^2}{4} + 4t^2\right)^{1/2}} \quad (9)$$

The dimensionless coupling constants are written as

$$\lambda = \psi(0){g_n}^2/\omega_n \quad (10)$$

It is the g_n which are the fundamental microscopic electron−molecular−vibration coupling constants. Interaction of the A_g phonon mode with the charge-transfer excitation causes the resonance frequency of the vibration to be shifted to lower frequency from its unperturbed position in an isolated molecule. Within the isolated dimer model, we can calculate

$$\text{Re}\left(\frac{1}{\sigma}\right) = A\left(B + \sum_n \frac{{g_n}^2\omega_n\gamma_n}{({\omega_n}^2 - \omega^2)^2 + (\omega\gamma_n)^2}\right) \quad (11)$$

where A and B are constants, relating to the dimensions of the unit cell and the electronic parameters, respectively. Thus, by fitting a sum of Lorentzian oscillators to this function, we can obtain the unperturbed frequencies of each A_g mode.[41]

A fit of this model to the ζ-(BEDT−TTF)PF$_6$ data is shown in Figure 11. The structural parameters used in the calculation were the separation between the BEDT−TTF molecules a = 3.524 Å and the unit-cell volume V_{cell} = 451 Å^3. The fitted parameters for the charge-transfer band are a transfer integral, t = 1700 cm^{-1}, and an effective Coulomb repulsion, U_{eff} = 6620 cm^{-1}. The charge-transfer energy and electronic line width are ω_{ct} = 7990 cm^{-1} and γ_{e} = 1900 cm^{-1}. The experimental values for the unperturbed phonon frequencies ω_n, EMV coupling constants g_n, and dimensionless electron−phonon coupling constants λ_n are listed in Table 5.

As shown in Figure 11 and Table 5 we have assigned the highest-frequency EMV vibrational features at ∼2986 and 2934 cm^{-1} to the totally symmetric C−H stretching BEDT−TTF motion: ν_1 and ν_2. The strongest interaction between the electronic system and the intramolecular A_g vibrations is manifested by the modes in the 1400 cm^{-1} range. The peak at ∼1447 cm^{-1} is probably connected with the ring C=C stretching

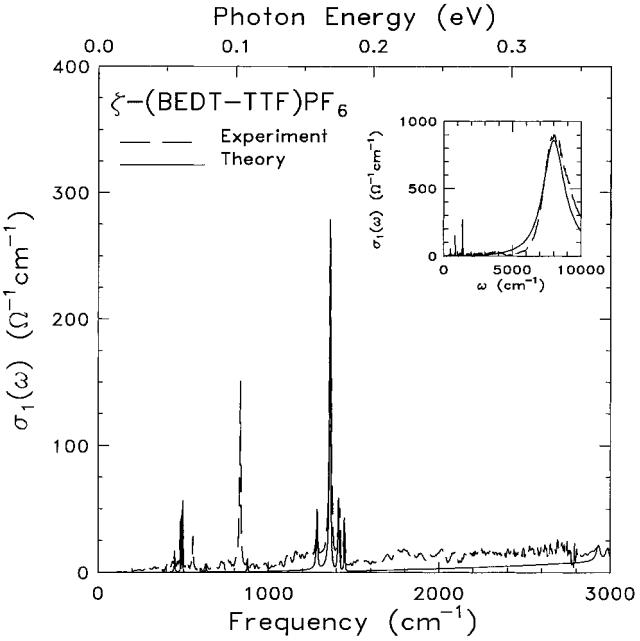

Figure 11. Isolated dimer fit (solid line) to the frequency-dependent conductivity (dashed line) of ζ-(BEDT−TTF)PF$_6$. Inset shows the conductivity in the range up to 10 000 cm^{-1}.

Table 5. Electron−Molecular−Vibration Coupling Parameters for ζ-(BEDT−TTF)PF$_6$

ω_n[a] (cm^{-1})	g_n (cm^{-1})	λ_n
2986	140	0.001
2934	145	0.001
1452	300	0.009
1425	235	0.006
1420	350	0.013
1385	450	0.022
1290	180	0.004
878	100	0.002
636	100	0.002
502	250	0.020
494	130	0.005
485	90	0.003
452	155	0.008
	total	0.096

[a] Obtained from plot of Re[1/$\sigma(\omega)$].

$A_g(\nu_3)$. The bands close to 1420, 1412, and 1360 cm^{-1} are due to EMV coupling of the A_g mode which involves the central C=C stretching (ν_4). It should be noted that the calculated EMV coupling constants for these modes are the greatest of any A_g mode. The mode near 1287 cm^{-1} is believed to be either H−C−H bending $A_g(\nu_5)$ or C−C−H bending $A_g(\nu_6)$. The bands that are of unambiguous origin from 900 to 600 cm^{-1} are the two C−S stretching modes $A_g(\nu_{10},\nu_{11})$ at ∼878 and 636 cm^{-1}. The next largest features are in the group near 500 cm^{-1}, which have been assigned to the C−S stretching $A_g(\nu_{12})$ and which appear as a triple mode at ∼502, 494, and 485 cm^{-1}. Certainly $A_g(\nu_{12})$ is calculated to have the second-largest EMV coupling constant. The remaining mode at ∼452 cm^{-1} is the C−S stretching $A_g(\nu_{13})$.

(2) Low-Temperature Data. As mentioned above, the far-infrared spectrum of ζ-(BEDT−TTF)PF$_6$ has several strongly temperature-dependent vibrational features polarized along the *a* axis. Some of these modes are readily understood as arising from EMV coupling. Here, we will concentrate on the temperature behavior of the A_g modes below 600 cm^{-1} shown in Figure 8. The character of the triple mode at ∼498, 491, and 482 cm^{-1}

(41) Yartsev, V. M.; Jacobsen, C. S. *Phys. Status Solidi* **1988**, *B125*, K149.

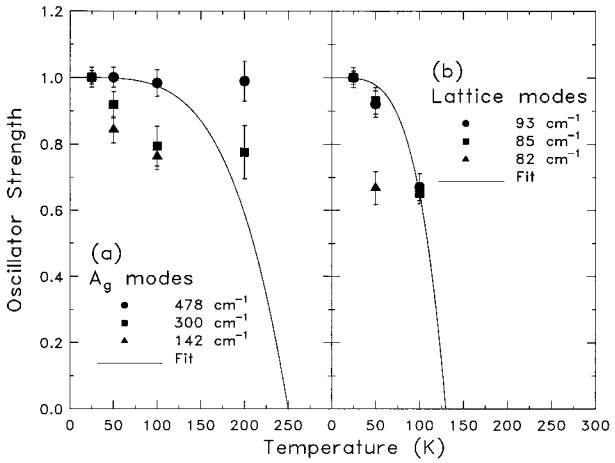

Figure 12. Normalized oscillator strength of (a) three A_g modes, and (b) three lattice modes of ζ-(BEDT−TTF)PF_6 vs temperature. The solid line is a fit using the temperature dependence of the BCS (mean-field) order parameter.

and a single mode near 450 cm^{-1} is primarily C−S stretching (ν_{12}). Strikingly, these A_g phonon components disappear when the crystal is cooled from 300 to 200 K. At the same time, several new A_g phonon modes at ∼478, 300, and 142 cm^{-1} are seen in the low-temperature phase. The peaks at ∼300 and 142 cm^{-1} are the exterior ring deformation (ν_{15}) and interior ring deformation (ν_{16}), respectively. The oscillator strengths of these lowest-frequency A_g modes are plotted in Figure 12a versus the temperature. These data have been normalized with respect to their 25 K value. As can be seen, the spectral weight of the 478 and 300 cm^{-1} modes changes in a relatively gradual and continuous manner with increasing temperature. Above 200 K, both decrease to zero. In contrast, the 142 cm^{-1} mode displays a stronger temperature variation in the low-temperature phase and is sharply reduced as temperature is increased higher than 100 K. These results highlight the important connection between the electron−phonon coupling and PF_6^- anion ordering transition.

The low-energy features below 100 cm^{-1} display strong temperature and polarization dependence as well. We have tentatively classified them as intermolecular lattice modes. In general, these intermolecular modes are more difficult to assign than their intramolecular counterparts because of their weak intensity, broadening at higher temperature, and the strong dependence of their frequencies on the lattice structure. However, the observed temperature and polarization dependence are useful criteria for distinguishing between a very low energy intramolecular or a lattice mode. The assignments also rely upon low-energy Raman measurements.[42] We show in Figure 12b the behavior of three lattice modes at ∼93, 85, and 82 cm^{-1} as a function of temperature. The oscillator strength of the 93 and 85 cm^{-1} modes decreases slowly between 50 and 100 K and is zero by 200 K. In addition, the 82 cm^{-1} lattice mode decreases above 50 K and is not observed at 100 K. These modes may be implicated in the magnetic phase transition discussed later.

(D) Anion Ordering Transition. We will now turn to a discussion on the nature of the phase transitions in ζ-(BEDT−TTF)PF_6. The high-temperature transition, observed near 250 K in dc conductivity and magnetic susceptibility measurements, is a structural transition associated with ordering of the PF_6^- ions within the anion sheet. Optical and X-ray structure results taken above and below the transition temperature are consistent with loss of the PF_6^- anion rotational disorder as the temperature is lowered. The room-temperature X-ray data require random occupancy of two rotational orientations for the PF_6^- anion while in the 173 K structure the anions are fixed.

The anion ordering results in slight changes in the intermolecular interactions between BEDT−TTF cations. While the $P\bar{1}$ space group is unchanged and the mode of intermolecular overlap is unaffected by anion ordering, there is a decrease in S−S contacts along the *a* axis from 3.525 Å at 298 K to 3.470 Å at 173 K and along the diagonal of the *ab* plane from 3.523 Å at 298 K to 3.424 Å at 173 K. The calculated β interaction energies along the *a* axis, *b* axis, and the diagonal of the *ab*-plane at 173 K are 0.209, 0.108, and 0.006 eV, respectively. Thus, the enhanced intermolecular contacts lead to a slight increase of the HOMO−HOMO interactions along the *a* axis and *b* axis which is also seen in the transport measurements as a change in activation energy, decreasing from 0.30 to 0.23 eV below the crossover point near 250 K. This behavior suggests that the barrier to hopping of the localized electrons is decreased in the anion ordered phase. There is also a gradual decrease in the magnetic susceptibility in the vicinity of the order/disorder transition. Increased antiferromagnetic exchange as the donor molecules move closer results in a lowering of the magnetic susceptibility.

The anion ordering phase transition is also seen in the temperature-dependent behavior of the vibrational structures of the PF_6^- anions. The infrared-active phonons seen at ∼556 and 883 cm^{-1} for both polarizations in Figures 4 and 8 are the PF_6^- ion bending ν_4(F_{1u}) and stretching ν_3(F_{1u}) modes. The temperature dependence of the center frequency, line width, and oscillator strength of the bending mode (from fits to Lorentz oscillators) are displayed in Figure 13. Errors in the parameters are ±5%. We note two effects: (1) A reduction of γ (decrease in the damping) as the temperature of the sample is decreased from 300 to 200 K, with some saturation in γ below 200 K, and (2) there is a splitting of the modes for both polarizations as the temperature is lowered. These figures clearly indicate that the PF_6^- anions freeze into position below the order/disorder structural transition.

The changes in the electron−phonon coupling between the high- and low-temperature phases has already been discussed. This interaction is fundamentally related to changes in the lattice distortion and electronic configuration. As already shown in Figure 8a, the strong triple A_g mode near 500 cm^{-1} disappears upon cooling from room temperature to 200 K and is replaced by a single strong mode. This result indicates that there is a change of the environment of the BEDT−TTF molecules in the low-temperature phase, directly connected with the ordering of the PF_6^- counterions. This change may be attributed to the reduced distance between the BEDT−TTF donors along the crystallographic *a*-axis in the low-temperature structure.

(42) Eldridge, J. E.; Homes, C. H.; Williams, J. M.; Kini, A. M.; Wang, H. H. *Spectrochim. Acta* **1995**, *51A*, 947.

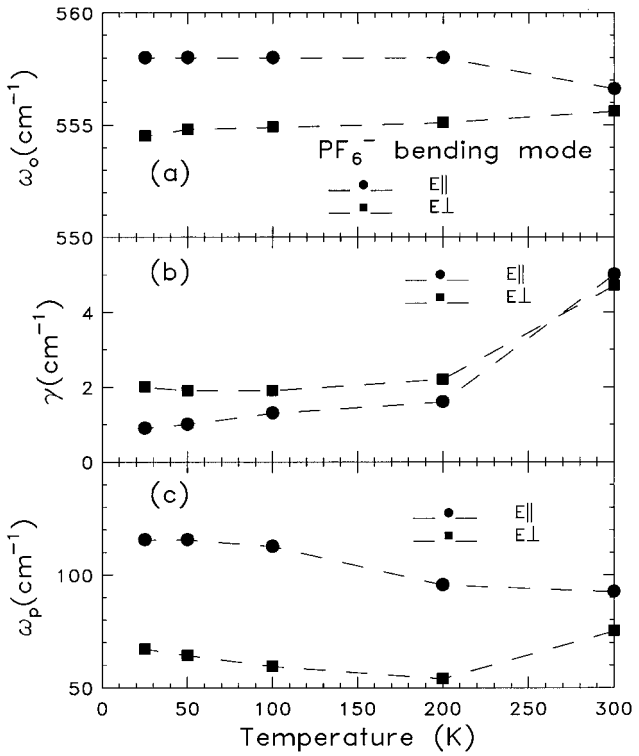

Figure 13. Temperature dependence of (a) center frequency ω_0, (b) line width γ, and (c) oscillator strength ω_p of PF_6 anion bending mode for two different polarizations.

The A_g intramolecular vibration spectra are also useful for investigating the dynamic aspects of the phase transition. In particular, they allow study of the amplitude of the charge-density distortion or lattice dimerization: a strong lattice distortion results in a charge density wave with a large amplitude and consequently strong activation of the vibrational modes of proper symmetry; a weak or nonexistent lattice distortion results in little or no activation.

The temperature dependence of the order parameter, Δ, rather than the effective lattice dimerization, is actually the more fundamental quantity with which to probe the nature of the charge-density wave. Bozio and Pecile[43,44] have discussed the relationship between the A_g phonon mode oscillator strengths and the order parameter. They find the oscillator strength of the totally symmetric vibrational modes to be proportional to Δ^2. We have analyzed the optical data presented in Figure 12a along these lines. The solid line in Figure 10a shows a phenomenological curve:

$$\frac{N_{\text{eff}}}{N_0} = \frac{\omega_p^{\,2}(T)}{\omega_p^{\,2}(0)} = \left[\frac{\Delta(T)}{\Delta(0)}\right]^2 \tag{12}$$

where we have used $\Delta(T)$ as the temperature dependence of the (mean-field) BCS order parameter. This assumption gives a nearly constant $\Delta(T)$ at $T \ll T_c$; near T_c, $\Delta(T)$ drops to zero with a $(1 - T/T_c)^{1/2}$ behavior. Taking $T_c = 250$ K, the normalized oscillator strength of the three lowest-frequency A_g bands agrees with this expression. We can conclude from the gradual variation of the integrated spectral intensity of the 478, 300, and 142 cm^{-1} A_g modes in ζ-(BEDT−TTF)PF_6 with temperature that the order parameter of the phase transition changes gradually with temperature in this compound. The previously discussed changes in the dc conductivity and magnetic susceptibility were also gradual in this temperature range. Consequently, this high-temperature transition in ζ-(BEDT−TTF)PF_6 can be described as a second-order process.

(E) Magnetic Phase Transition. The most striking feature in the magnetic susceptibility data of Figure 9 is the exponential drop in susceptibility toward zero at $T < 40$ K. The slight increase of the χ value at $T < 10$ K obeys the Curie law and is believed to be extrinsic in origin. For reasons discussed below, we have treated the 40 K drop in susceptibility as a spin-Peierls transition. The general approach to analysis the data will be similar to those[45−51] that have followed the Hartree−Fock predictions of Bulaevskii,[52] with additional input from Pytte.[53]

The magnetic transition temperature, T_{sp}, is defined by the kink in the susceptibility vs temperature plot. The finite energy gap is assumed to have the usual BCS temperature dependence, and in the ground state it is given by

$$\Delta(0) = 1.76 k_B T_{sp} \tag{13}$$

We assume that $J = 4T_{sp}$, since the expression provided by Bulaevksii[52] is valid for $T/J < 0.25$. Below T_{sp} two alternating J's $[J_{1,2}(T)]$ are formed and expressed as

$$J_{1,2}(T) = J[1 \pm \delta(T)] \tag{14}$$

According to the mean-field theory of Pytte[53] the relationship between $\delta(T)$ and the excitation energy gap $\Delta(T)$ at temperature T is found from

$$\delta(T) = \Delta(T)/pJ \tag{15}$$

where the value of p is 1.637. The above choices define the parameters needed for obtaining a theoretical fitting for $\chi(T < T_{sp})$. The estimate of $\chi(T_{sp})$ is multiplied by a factor to scale its value to the one observed experimentally at T_c,[48] where simultaneously adding a $\chi(0)$ term as needed. Finally, the Curie term is adjusted to the data near T_{min}, although it plays a rather small role in the fit near T_{sp}. Given these conditions, the results for the fit are compared to the data in the inset of Figure 9. Within reasonable choices of the parameters in Table 4 and the uncertainty of the measurement, this spin-Peierls model reproduces the experimental data.

(43) Bozio, R.; Pecile, C. *J. Phys. C* **1980**, *13*, 6205.
(44) Bozio, R.; Pecile, C. *Solid State Commun.* **1981**, *37*, 193.
(45) Bray, J. W.; Interrante, L. V.; Jacobs, I. S.; Bonner, J. C. In *Extended Linear Chain Compounds*; Miller, J. S., Ed.; Plenum: New York, 1983; Vol. 3, Chapter 7.
(46) Bray, J. W.; Hart, H. R., Jr.; Interrante, L. V.; Jacobs, I. S.; Kasper, J. S.; Watkins, G. D.; Wee, S. H.; Bonner, J. C. *Phys. Rev. Lett.* **1975**, *35*, 744.
(47) Jacobs, I. S.; Bray, J. W.; Hart Jr., H. R.; Interrante, L. V.; Kasper, J. S.; Watkins, G. D.; Prober, D. E.; Bonner, J. C. *Phys. Rev. B* **1976**, *14*, 3036.
(48) Huizinga, S.; Kommandeur, J.; Sawatzky, G. A.; Thole, B. T.; Kopinga, K.; de Jonge, W. J. M.; Roos, J. *Phys. Rev. B* **1979**, *19*, 4723.
(49) Obertelli, S. D.; Friend, R. H.; Talham, D. R.; Kurmoo, M.; Day, P. *J. Phys. Condens. Matter* **1989**, *1*, 5671.
(50) Jacobsen, C. S.; Pederson, H. J.; Mortensen, K.; Bechgaard, K. *J. Phys. C: Solid State Phys.* **1980**, *13*, 3411.
(51) Hase, M.; Terasaki, L.; Uchinokura, K. *Phys. Rev. Lett.* **1993**, *70*, 3651.
(52) Bulaevskii, L. N. *Fiz. Tver. Tela* **1969**, *11*, 1132 [*Sov. Phys. Solid State* **1969**, *11*, 921].
(53) Pytte, E. *Phys. Rev. B* **1974**, *10*, 4637.

As the temperature is lowered in a quasi-one-dimensional Heisenberg antiferromagnet, there is a competition between a three-dimensional ordered antiferromagnetic state and the spin-Peierls ground state. On the basis of magnetic susceptibility data alone, it can be difficult to distinguish between the two ground states. Although χ for an ordered antiferromagnet is anisotropic, in powder samples χ rapidly decreases below the ordering temperature for both antiferromagnetic and spin-Peierls states. However the temperature dependence of χ is different in the two cases below T_{sp}, and the susceptibility of ζ-(BEDT−TTF)PF_6 is nicely fit by a spin-Peierls model, as seen in Figure 9. The ESR behavior is also consistent with a spin-Peierls transition. The ESR line width decreases as the temperature is lowered toward T_{sp}, below which the X-band signal rapidly disappears and is no longer present at 30 K. On the other hand, for systems approaching antiferromagnetic order, the ESR behavior is expected to be different. Pretransitional antiferromagnetic fluctuations cause a rapid divergence of the ESR line width as the temperature decreases toward the Neel temperature T_N and the ESR signal becomes too broad to observe just above the ordering transition. Below T_N, antiferromagnetic resonance modes, if observable, will be far removed from the $g = 2$ lines seen above the transition. In the spin-Peierls case, dimerization proceeds progressively below T_{sp}, resulting eventually in a nonmagnetic state. The system remains paramagnetic just below T_{sp} until the magnetic gap becomes too large as the temperature is decreased further. The observation of a narrow ESR line at and just below the transition temperature is consistent with the spin-Peierls assignment.

Unlike antiferromagnetic ordering, the spin-Peierls transition is a structural transition. Qualitatively, the spin-Peierls transition can be described as a magnetoelastic transition whereby one-dimensional spin chains couple to a three-dimensional phonon, resulting in the spin−lattice dimerization proceeding continuously and progressively below the transition temperature. While the dimerization should be seen below T_{sp}, precursive lattice softening is often observed at temperature well above T_{sp}. Precursive effects were seen in the first reported spin-Peierls system, the metal bisdithiolene complexes of tetrathiafulvalene (TTF),[46,47] (TTF)$Cu(S_2C_2(CF_3)_2)_2$ and (TTF)$Au(S_2C_2(CF_3)_2)_2$ which have T_{sp} of 12 and 2.1 K, respectively. A diffuse X-ray study of (TTF)$Cu(S_2C_2(CF_3)_2)_2$ above T_{sp} shows the persistence, up to at least 225 K, of enhanced scattering at the position of the new Bragg peaks seen below T_{sp}. This scattering was found to be approximately isotropic in k space, indicating that the implied precursive lattice softening is fully three-dimensional. The apparently fortuitous existence of this soft phonon mode at the wave vector ($2k_F$) appropriate for lattice dimerization facilitates the occurrence of the spin-Peierls transition. We have not performed structural analyses below 40 K on ζ-(BEDT−TTF)PF_6, but the appearance of new intermolecular vibrational modes at temperature above T_{sp} are evidence for three-dimensional lattice softening of a lattice mode compatible with spin-Peierls dimerization. Three new lattice modes near 93, 85, and 82 cm^{-1} become observable at temperatures above T_{sp} and increase oscillator strength as the temperature is lowered. The temperature dependence of the vibrational intensities are shown in Figure 12b. Their appearance is reminiscent of precursor effects seen in other spin-Peierls materials and is consistent with the assignment of the 40 K magnetic transition to a spin-Peierls transition.

Spin-Peierls transitions have been observed in several other molecular solids. Some examples include the TCNQ salt MEM$(TCNQ)_2$[48] (MEM is the methylmorpholinium cation), the cation radical salt $(TMTTF)_2PF_6$[54−56] (TMTTF is tetramethyltetrathiafulvalene), and (BEDT−TTF)$_2Ag(CN)_2$.[49] In each case a high-temperature structural transition or structural pretransitional fluctuation was observed at temperatures well above T_{sp}. While the spin-Peierls state is most commonly seen in molecular solids, a spin-Peierls transition was recently discovered in the purely inorganic compound $CuGeO_3$.[51,57−59]

A final point to consider is the role of the Peierls transition in the Hubbard model for a half-filled band. For $U = 0$, the charge and spin degrees of freedom are unseparated and the Peierls transition opens equal gaps for both the charge and magnetic excitations by means of a lattice distortion at $2k_F$. As U increases, a new instability appears at $4k_F$ which is chiefly associated with electron localization and therefore with reduction of the charge degrees of freedom. The $2k_F$ instability remains but becomes more associated with the spin degrees of freedom as U increases, gradually evolving into a spin-Peierls transition for $U \gg t$. In the case of ζ-(BEDT−TTF)PF_6, all physical properties demonstrate that this material is a magnetic insulator of the Mott−Hubbard type. In light of the large value $U \gg t$, it would seem then that the charge degrees of freedom are frozen out even at high T, with strong localization of the charge carriers. Then, the spin degrees of freedom are lost at low temperature. Thus, the ground state of ζ-(BEDT−TTF)PF_6 can be considered as a $2k_F$ spin-Peierls state.

V. Summary

In summary, a new 1:1 cation-radical salt, ζ-(BEDT−TTF)PF_6, has been synthesized and characterized. Its physical properties demonstrate that this material is a magnetic insulator of the Mott−Hubbard type. From an analysis of the frequency-dependent optical conductivity we obtain values for the effective on-site Coulomb repulsion $U_{eff} = 0.82$ eV, and for the transfer matrix element $t = 0.21$ eV. ζ-(BEDT−TTF)PF_6 would fall into the intermediate-to-strong Coulomb correlation case because of $U_{eff} \sim 4t$. The a axis conductivity shows the effects of electron−molecular−vibration interaction with a dimensionless electron−phonon coupling constant $\lambda \sim 0.1$.

Upon comparison of the structural, transport, optical, and magnetic properties of ζ-(BEDT−TTF)PF_6, it be-

(54) Maaroufi, A.; Flandrois, S.; Coulon, C.; Delhaes, P.; Morand, J. P.; Fillion, G. *J. Phys. Colloid* **1983**, *44*, C3, 1091.
(55) Creuzet, F.; Boubonais, C.; Caron, L. G.; Jerome, D.; Bechgaard, K. *Synth. Met.* **1984**, *19*, 289.
(56) Creuzet, F.; Jerome, D.; Moradpour, A. *Mol. Cryst. Liq. Cryst.* **1985**, *119*, 297.
(57) Hase, M.; Terasaki, I.; Uchinokura, K.; Tokunaga, M.; Miura, N.; Obara, H. *Phys. Rev. B* **1993**, *48*, 9616.
(58) Pouget, J. P.; Regnault, L. P.; Ain, M.; Hennion, B.; Renard, J. P.; Veillet, P.; Dhalenne, G.; Revcolevschi, A. *Phys. Rev. Lett.* **1994**, *72*, 4037.
(59) Musfeldt, J. L.; Wang, Y. J.; Jandl, S.; Poirier, M.; Pevcolevschi, A.; Dhalenne, G. *Phys. Rev. B* **1996**, *54*, 469.

comes clear that this salt exhibits successive phase transitions. A direct observation of ordering of PF_6^- anions has been obtained by means of X-ray diffraction measurements at 173 K. The net effect of this order/disorder transition is to reduce the value of the transport activation energy below 250 K and to cause the magnetic susceptibility to decrease in a continuous manner from 300 to 200 K, with a very small discontinuity at 250 K. The optical results showing a splitting of the PF_6^- bending vibration and the change from a triple to a single A_g mode of BEDT−TTF donor molecule near 500 cm^{-1} are also observed in this temperature region. Moreover, the temperature dependence of the A_g mode intensity shows a characteristic second-order-like behavior at $T_c = 250$ K, being nearly constant at $T < T_c$, associated with a gradual change through T_c.

In the low-temperature phase, the spin-Peierls transition can be characterized by a sudden drop of χ at $T_{sp} \sim 40$ K. However, the optical evidence for a structural modification of ζ-(BEDT−TTF)PF_6 occurs at temperatures higher than T_{sp} (up to 130 K). The presence of three lattice modes in the far-infrared is the main vibrational change that gets involved in the magnetic phase transition. This effect is a precursive three-dimensional softening of the phonon corresponding to the eventual spin-Peierls dimerization. The softening phenomenon facilitates spin−phonon coupling and appears to be associated with a structural transition in ζ-(BEDT−TTF)PF_6.

Acknowledgment. This work was supported in part by the National Science Foundation, Grants DMR-9403894 (H.L.L. and D.B.T.), and DMR-9530453 (D.R.T.) DMR-9200671 (G.E.G. and M.W.M). Partial support for D.R.T. from the donors of the Petroleum Research Fund, administrated by the ACS, is also acknowledged. We thank Prof. J. R. Childress for making the SQUID magnetometer, acquired through an NSF instrumentation grant, DMR-9422192, available for our use.

Supporting Information Available: Full details of the crystal structure characterization, atomic coordinates, bond lengths and angles, and anisotropic temperature factors have been deposited as Supporting Information and to the Cambridge Crystallographic Data Centre (13 pages). Ordering information is given on any current masthead page.

CM970143T